NANO LETTERS
Letter
Cite This: Nano Lett. 2018, 18, 4710−4715
pubs.acs.org/NanoLett

Stark Tuning of Single-Photon Emitters in Hexagonal Boron Nitride

Gichang Noh,[†] Daebok Choi,[†] Jin-Hun Kim,[‡] Dong-Gil Im,[‡] Yoon-Ho Kim,[‡] Hosung Seo,[†] and Jieun Lee*,[†]

[†]Department of Physics and Department of Energy Systems Research, Ajou University, Suwon 16499, Korea
[‡]Department of Physics, Pohang University of Science and Technology (POSTECH), Pohang 37673, Korea

Supporting Information

ABSTRACT: Single-photon emitters play an essential role in quantum technologies, including quantum computing and quantum communications. Atomic defects in hexagonal boron nitride (*h*-BN) have recently emerged as new room-temperature single-photon emitters in solid-state systems, but the development of scalable and tunable *h*-BN single-photon emitters requires external methods that can control the emission energy of individual defects. Here, by fabricating van der Waals heterostructures of *h*-BN and graphene, we demonstrate the electrical control of single-photon emission from atomic defects in *h*-BN via the Stark effect. By applying an out-of-plane electric field through graphene gates, we observed Stark shifts as large as 5.4 nm per GV/m. The Stark shift generated upon a vertical electric field suggests the existence of out-of-plane dipole moments associated with atomic defect emitters, which is supported by first-principles theoretical calculations. Furthermore, we found field-induced discrete modification and stabilization of emission intensity, which were reversibly controllable with an external electric field.

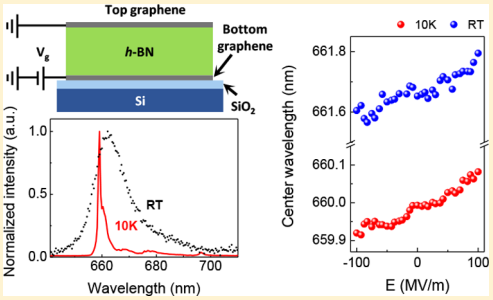

KEYWORDS: *Single-photon sources, hexagonal boron nitride, Stark effect, van der Waals heterostructures*

Two-dimensional (2D) materials have emerged as new candidates for the building blocks of quantum devices because of their unique electronic and optical properties.[1,2] Recent reports on single-photon emitters (SPE) in transition-metal dichalcogenides (TMDCs)[3−6] and hexagonal boron nitride (*h*-BN)[7−13] have drawn significant interest regarding 2D materials for quantum information processing. However, single photons generated from different emitters show inhomogeneous energy distribution, which would be detrimental for potential applications in quantum communications. There has been great interest in overcoming the inhomogeneity of SPE in these materials (for example, by optimizing the fabrication process[11,12] or by tuning the SPE's optical energy through applying strain[13] or using the Stark effect[14]). In the Stark effect, the optical energy of each SPE could shift by the application of an external electric field, which is advantageous for the local control of individual emitters. The method has been demonstrated for SPE in TMDC monolayers at low temperatures.[14] For practical and more-versatile applications of 2D-based quantum photonics, however, it is necessary to integrate SPE operation at room temperature into devices with tunable electric fields.

h-BN is a wide-bandgap semiconductor (E_{gap} = 6 eV),[15] in which deep-level atomic defects produce single-photon emissions at room temperature. The structure of *h*-BN consists of single *h*-BN layers that are weakly coupled by van der Waals force in the vertical direction, appropriate for the fabrication of 2D heterostructures.[1] According to previous reports, native point defects in this system are normally expected to lie within the plane,[7] which could create an in-plane dipole that would be difficult to control with out-of-plane electric fields. However, for tunable and scalable *h*-BN SPE with a large density, it is highly desirable to be able to control individual atomic defects using an out-of-plane electric field. In this work, we fabricate *h*-BN/graphene heterostructures to apply an out-of-plane electric field to atomic defects in *h*-BN and observe linear Stark shifts up to 5.4 nm per GV/m. First-principles theoretical calculations provide a possible origin of the observed Stark shifts induced by out-of-plane electric fields. In addition, by applying a high gate voltage, we observe the discrete change of a defect's emitter intensity, reversibly controlled by an applied electric field. These results show the potential of *h*-BN/graphene heterostructures as tunable room-temperature quantum light sources integrated in electrical circuit assemblies for scalable solid-state quantum technologies.[16]

To produce *h*-BN defect centers, we annealed physically exfoliated *h*-BN flakes with thickness ranging between 100 and 200 nm in a chamber filled with argon (P = 500 mTorr) at 800 °C for 30 min.[7] We then employed a microphotoluminescence (μPL) measurement on annealed *h*-BN using a 532 nm continuous-wave laser to find flakes with bright and stable emitters. With *h*-BN flakes containing emitters, two graphene/*h*-BN/graphene heterostructures (device A and B; Figure S1) are fabricated to apply vertical electric fields, as shown in

Received: March 14, 2018
Revised: May 22, 2018
Published: June 22, 2018

Downloaded via POHANG UNIV OF SCIENCE & TECHNOLOGY on December 21, 2020 at 04:47:36 (UTC).
See https://pubs.acs.org/sharingguidelines for options on how to legitimately share published articles.

© 2018 American Chemical Society

DOI: 10.1021/acs.nanolett.8b01030
Nano Lett. 2018, 18, 4710−4715

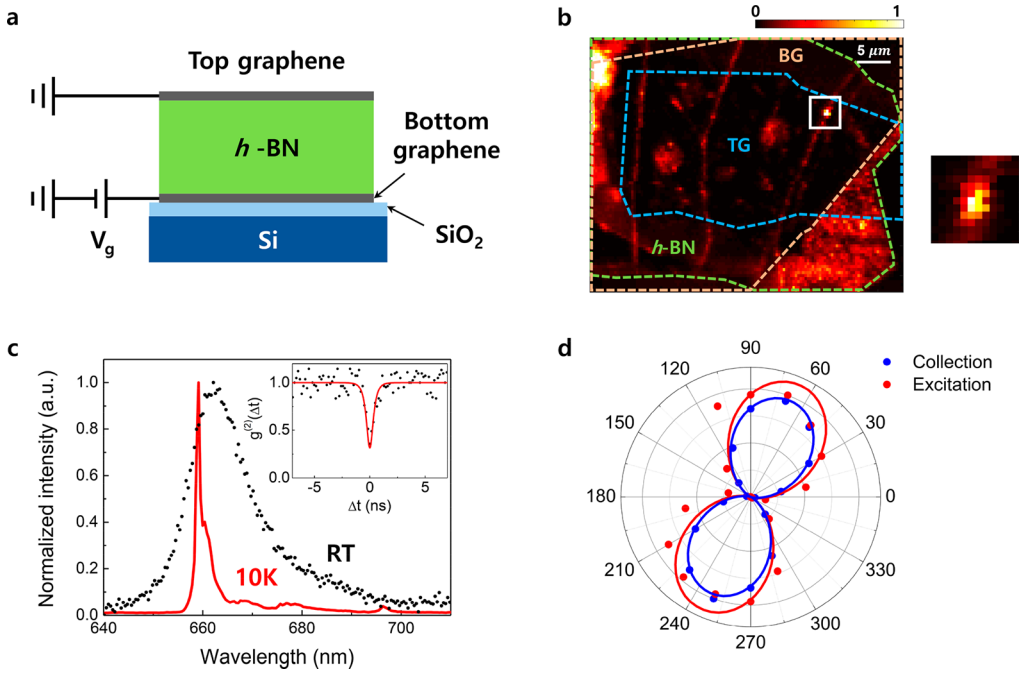

Figure 1. Single-photon emission from a point defect in graphene/*h*-BN/graphene heterostructures. (a) Device schematics of multilayer *h*-BN sandwiched by top and bottom few-layer graphene. (b) Scanning photoluminescence image of device A measured at 10 K. The squared bright spot shows a localized defect emission. The boundaries of top graphene (TG), *h*-BN, and bottom graphene (BG) are shown by dashed lines. (c) Photoluminescence spectrum of the emitter shown in panel b measured at 10 K and room temperature. In the inset is the second-order correlation ($g^{(2)}(\Delta t)$) function of the emitter showing single photon purity of $g^{(2)}(0) = 0.3$. (d) Emission-intensity dependence on excitation laser polarization (red dots) and collection polarization (blue dots). The red and blue solid lines are fit lines to $\sin^2(\theta)$.

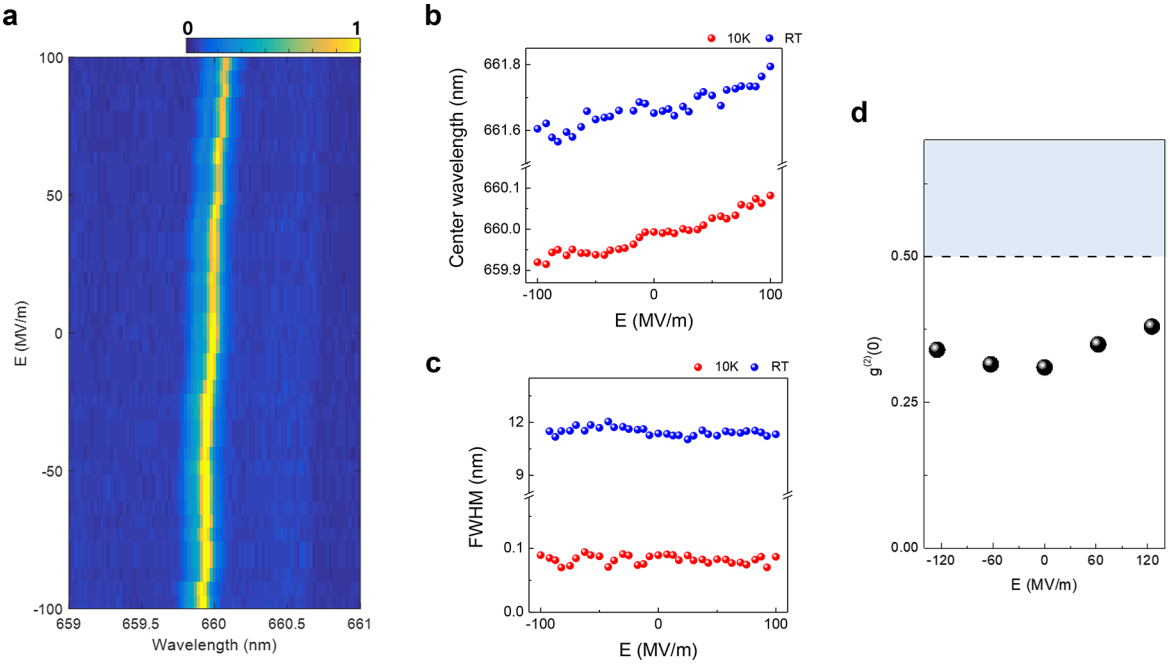

Figure 2. Stark shift of the single-photon emitter (SPE) shown in Figure 1. (a) Color plot of photoluminescence spectra of the SPE as a function of out-of-plane electric field measured at 10 K. The bright yellow color shows the peak wavelength shifting with the applied electric field. (b) The center wavelength shift of the emitter at 10 K (red dots) and room temperature (blue dots) under varying electric fields. (c) The full width at half-maximum of the emitter at 10 K (red dots) and room temperature (blue dots). (d) Second-order correlation function $g^{(2)}(0)$ measured at selected fields at 10 K.

Figure 1a. In the fabrication process, polypropylene carbonate (PPC) is used to dry-transfer each few-layer (FL) graphene and *h*-BN onto 100 nm thick SiO_2 substrates with prepatterned Ti/Au electrodes.[17] We have chosen graphene with similar thicknesses for symmetric gating electrodes. By applying a voltage (V_g) between the Au electrodes contacting top and bottom graphene, a vertical electric field (E) is applied to the emitters. The actual field applied is $E = \frac{(\varepsilon_{BN}+2)V_g}{3t}$ according to

DOI: 10.1021/acs.nanolett.8b01030
Nano Lett. 2018, 18, 4710−4715

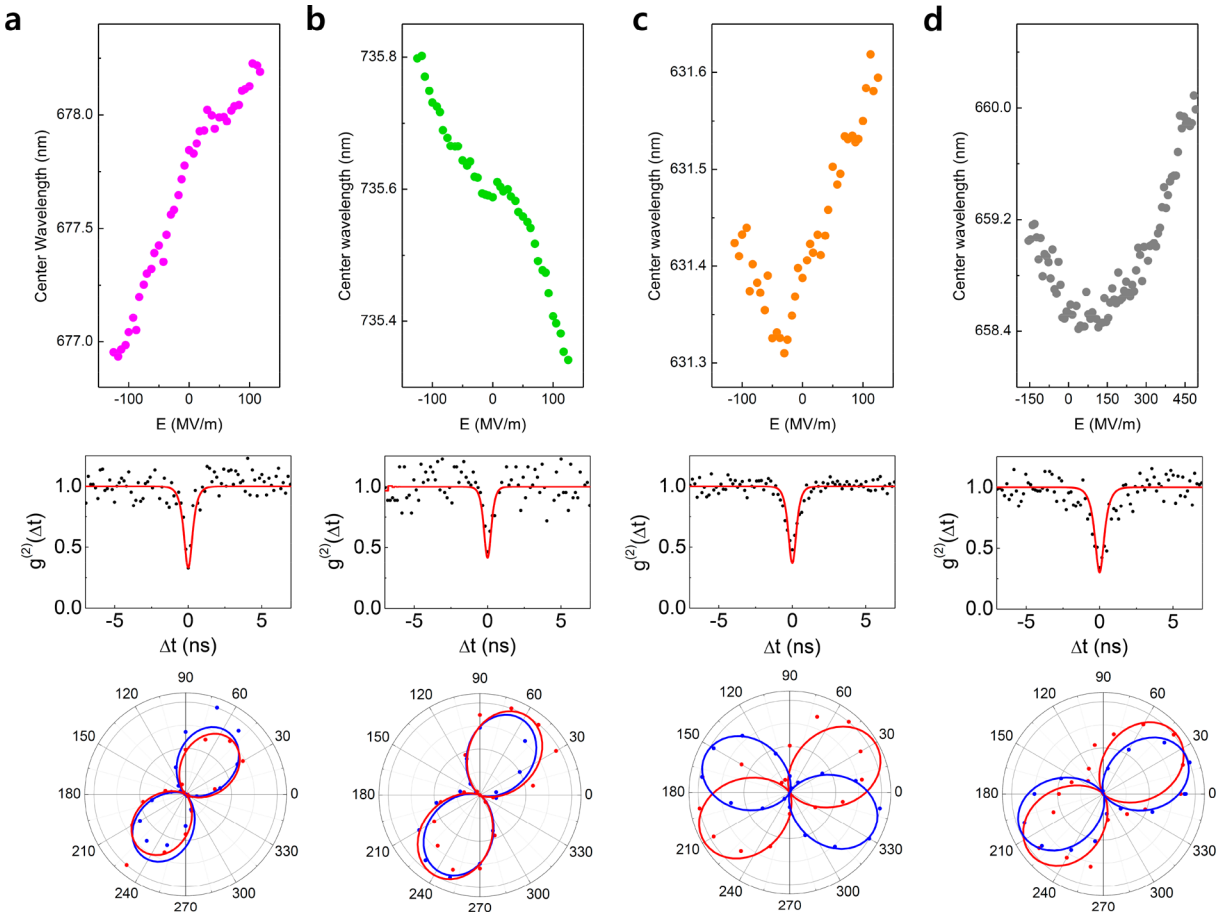

Figure 3. Various types of Stark shifts in different emitters. (a, b) Linear Stark shift observed from two different defects in device A, each showing $\Delta\mu$ of (a) 0.9 D and (b) −0.19 D, respectively. (c) V-shaped Stark shift measured from a defect in device A. The extracted $|\Delta\mu|$ is 0.24 D. (d) Quadratic Stark shift measured from a defect in device B. The extracted $\Delta\alpha$ and $\Delta\mu$ are 149 $Å^3$ and −0.22 D, respectively. The corresponding $g^{(2)}(\Delta t)$ function and polarization dependence (red dots: excitation, blue dots: collection) are also shown for each emitter.

the Lorentz local field approximation, in which ε_{BN} and t are the permittivity and thickness of *h*-BN, respectively.

We then performed a scanning μPL to map out the positions of bright emitters on device A, as shown in Figure 1b. The emission peak in Figure 1c shows the characteristic zero-phonon line (ZPL) of a defect. The second-order correlation measurement of the ZPL in the inset shows $g^{(2)}(0) = 0.3$, demonstrating the single-photon nature of the emitted light.[18] We also checked the emission-intensity dependence on the excitation laser polarization and collection polarization, respectively (Figure 1d). The linear-polarization dependence is obtained, indicating the anisotropy of the defect's crystal structure.[7] Together with the emission intensity saturation with increasing laser power (Figure S2), we confirm the quantum light emission characteristics of the defect center. All optical measurements are conducted at $T = 10$ K, where the emission line width is narrow except for some measurements at room temperature, used for testing the feasibility of our scheme in ambient conditions.

Next, we applied vertical electric fields to the SPE shown in Figure 1 and recorded the spectrum (Figure 2a). Surprisingly, the center wavelength shifts while applying out-of-plane electric fields, clearly showing the Stark-induced tuning of the SPE and the presence of an out-of-plane electric dipole associated with the SPE. By fitting the spectra to Lorentzian functions, we extracted the center wavelength and full width at half-maximum (fwhm) of the emission as a function of electric field, as shown in Figure 2b,c (details are given in Figure S3). The observed shift shows a linear dependence with a slope of 0.88 nm per GV/m. To double-check that the wavelength shift of the SPE is indeed induced by the applied electric field, we monitored the spectrum while reversing the bias direction by switching the gate and ground electrodes (Figure S4). There, the observed Stark shift changes the sign, ruling out the possibility that the wavelength shift is induced by the defect on the *h*-BN surface coupled to a nearby graphene. Moreover, the line width of the emission does not change much, and the extracted $g^{(2)}(0)$ values are below 0.5 in the given electric field range, demonstrating that the single-photon nature of the emitter is simultaneously maintained under the application of an electric field ($g^{(2)}(\Delta t)$ in Figure S5). In addition, the room temperature measurement of the same defect shows a similar Stark tuning to low-temperature results (Figure 2b blue circles), demonstrating the robustness of the SPE between 10 K and room temperature. Although line width broadening is observed at room temperature, the measured $g^{(2)}(0)$ equals 0.39 at $E = 0$ ($g^{(2)}(\Delta t)$ in Figure S6).

In Figure 3, we show various types of Stark shifts observed from different SPEs together with corresponding $g^{(2)}(\Delta t)$ and polarization dependence measurements. Figure 3a shows a SPE showing the same sign of the Stark shift to that shown in Figure 2 but with a generally larger slope of 5.4 nm per GV/m.

DOI: 10.1021/acs.nanolett.8b01030
Nano Lett. 2018, 18, 4710−4715

For another defect in the same *h*-BN (Figure 3b), we observed the opposite sign of linear Stark shift compared to Figure 3a under the same configuration of gating electrodes. The existence of a defect with such an opposite sign of the linear Stark shift provides an additional evidence that the measured SPEs are not on the surface but in the bulk of *h*-BN. Although the occurrence is lower than the linear cases, we have also observed defects with V-shaped and quadratic-shaped Stark shifts, as exemplified in panels c and d of Figure 3, respectively, possibly indicating the field-induced flipping of dipole orientation of defects. Detailed spectra data of each SPE can be found in Figure S7. By fitting the observed Stark shifts to the following equation, we extracted the dipole moment (μ) and polarizability (α) of defects in *h*-BN:

$$\Delta(\hbar\omega) = -\Delta\vec{\mu}\cdot\vec{E} - \vec{E}\cdot(\Delta\vec{\alpha}/2)\cdot\vec{E}$$

Here, $\hbar$ and ω are the Plank constant and photon frequency, respectively. From the fitting, we find the $\Delta\mu$ of the *h*-BN SPE to be distributed in a range from −0.9 to 0.9 D (1 D = 3.3 × 10^{-30} C · m). For the emitters exhibiting quadratic Stark shifts, the extracted $|\Delta\alpha|$ was within ∼150 Å^3. This $|\Delta\alpha|$ of SPE in *h*-BN is about 2 orders of magnitude smaller than that observed in diamond NV centers.[19] Because polarizability is proportional to the defect center's volume, such a small value of $|\Delta\alpha|$ may indicate the small volume and strongly bound electron wave functions in these defects.

To shed light on the origin of the linear Stark shifts observed in this system, we carried out first-principles density functional theory (DFT) calculations of potential SPEs in *h*-BN. In particular, we consider V_NX_B-type defects (X = C, N, or O) (see Figure 4a), which are considered as strong candidates of SPEs in *h*-BN.[7,20−25] To examine their Stark shifts, we first adopt the widely used C_{2v} structural models of V_NX_B-type defects.[7,20−25] Figure 4b shows the calculated ZPL shift of neutral V_NN_B as a function of out-of-plane electric field. We find, however, that the ZPL does not show any Stark shift. In the C_{2v} model of V_NN_B, the N impurity resides in the *h*-BN plane. Thus, the model does not possess any permanent dipole in the out-of-plane direction due to the inversion symmetry with respect to the *h*-BN plane, leading to the absence of a Stark shift upon the out-of-plane electric field.

Surprisingly, however, we found that the ground-state structure of neutral V_NX_B is not the widely used C_{2v} model,[7,20−25] but a reduced-symmetry C_{1h} structure. Figure 4c compares the energy of the C_{2v} and C_{1h} structures of the neutral V_NX_B defects (X = N, C, or O), which exhibits a significant energy lowering as the impurity atom (X_B) moves out of the plane, breaking the inversion symmetry. We also checked that this is true for neutral V_NX_B in the multilayer *h*-BN bulk. With the inversion symmetry broken, the defects develop a permanent dipole in the out-of-plane direction and exhibit linear Stark-induced ZPL shifts, as shown in Figure 4b. We note that the new C_{1h} models of the neutral V_NX_B defects are able to explain the essential features of the experimentally observed linear Stark shifts of the SPEs in *h*-BN, although the exact correspondence between the V_NX_B defects and the SPEs in *h*-BN has not been established yet.[7,20−25] First, we theoretically estimated $|\Delta\mu|$ of the neutral V_NX_B defects to be 0.36 D (V_NC_B), 0.27 D (V_NN_B), and 0.16 D (V_NO_B), which are on the same order of magnitude to our measurements. Second, there are two symmetrically equivalent structures for a C_{1h} V_NX_B defect: X_B atom being up or down (Δ = +1 or −1 in Figure 4c), leading to two possible out-of-plane dipole orientations, which are consistent with our observations (Figure 3a,b).

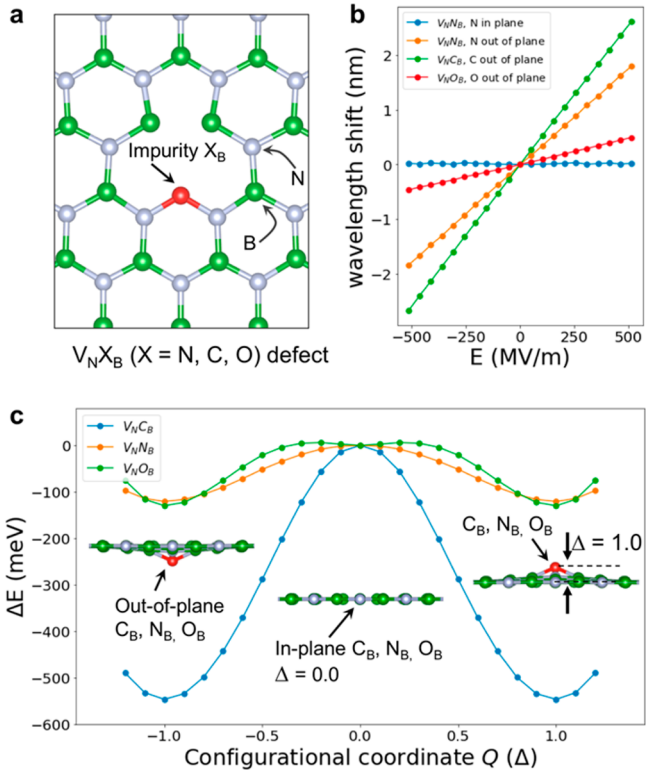

Figure 4. Density functional theory calculations of linear Stark effects. (a) Schematic of a V_NX_B defect, which is a pair of an impurity X substituting for boron atom (X_B) and its nearest neighboring N vacancy (V_N). (b) Theoretical ZPL shifts (ZPL(E) − ZPL(E = 0)) of neutral V_NX_B defects (X = C, N, or O) as a function of out-of-plane electric field (E). (c) Total energy of the V_NX_B (X = C, N, or O) defects as a function of configurational coordinate, which is mainly described by out-of-plane displacement of X_B. If the impurity atom (X_B) resides in-plane (Δ = 0), the symmetry of the defect is C_{2v} that has an inversion symmetry in the out-of-plane direction. However, if the impurity atom moves out-of-plane (Δ = ± 1), the inversion symmetry is broken, and the defect's symmetry is reduced to C_{1h}. The metastable Δ = 0 and the ground-state Δ = ± 1 structures are obtained by full DFT relaxations, while defect structures other than Δ = 0 and ±1 are generated by linear interpolation and extrapolation.

For the V-shaped Stark shift in Figure 3c, our results suggest that it may be related to structural transition between two possible defect orientations of the SPE. For the V_NX_B defects, their double-well potential shown in Figure 4c could become largely asymmetric in the presence of a strong electric field owing to the Stark coupling ($-\vec{d}\cdot\vec{E}$). This implies that, for a SPE with a shallow energy barrier, its defect structure could make a transition from one to the other upon reversing the electric field direction, leading to a flipping of its electric dipole. For the quadratic Stark shift observed in Figure 3d, however, the dipole flipping might be induced gradually with the application of an electric field. Such a quadratic dependence could arise for an emitter with non-degenerate excited states, which could be induced by strain or relative orientation of the defect to the electric field direction.[19] In addition, we found that the defects exhibiting nonlinear Stark shifts (Figure 3c,d) show rather larger misalignment of the excitation and emission dipole orientation compared with the ones showing linear Stark shifts (Figure 3a,b), possibly

DOI: 10.1021/acs.nanolett.8b01030
Nano Lett. 2018, 18, 4710−4715

suggesting the association of multiple excitation pathways for the dipole transitions in these defects,[26] which is a subject of further investigation.

Finally, in Figure 5, we present the electrical control of a defect in a device fabricated using single top graphene and bottom Si gates (device C). The detailed device image, spatial 2D map, polarization dependence, and laser power saturation of this defect are shown in Figure S10. By increasing the gate voltage from 0 to 60 V, we observe gate-induced discrete modification of the emission intensity at 46 V (Figure 5a). A real-time monitoring of the emitter with gate shows the reversibly controlled and stabilized emission intensity across the threshold voltage (Figure 5c). The observation can be attributed to the gate-induced charging effect, which is also observed in other solid-state emitters.[3,27] The gradual reduction of the threshold voltage with increasing laser power further supports the gate-induced charging, aided by photodoping through laser illumination (Figure 5d).

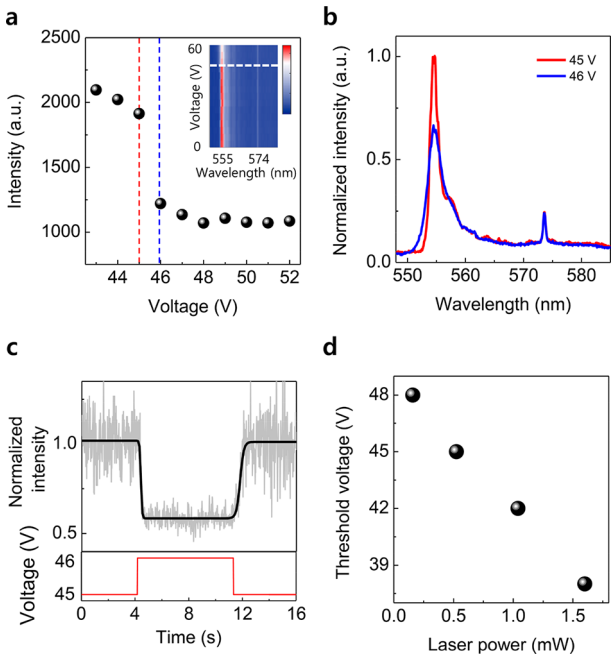

Figure 5. Gate-induced emission modification of a defect in device C. (a) Emission intensity of the defect while scanning the gate voltage for the laser power at 0.52 mW. Inset shows the color plot of the spectrum as a function of gate voltage. The white dashed line shows the threshold voltage. (b) Spectrum of the emitter at two different gates. The peak at 574 nm is *h*-BN Raman shift. (c) Time trace of the modified emission intensity (gray, upper) upon the change of the gate voltage (red, lower). The solid black line shows the fitting to a sigmoid function $I = (1 + e^{-k(t-t_0)})^{-1}$. (d) The threshold gate voltage measured at different excitation powers (Figure S11).

In summary, we have demonstrated the Stark-effect-induced energy control of atomic defects in *h*-BN by forming vertical heterostructures with graphene electrodes. The ability to induce Stark shifts up to 5.4 nm per GV/m is expected to benefit the preparation of two energetically identical single defects. From the linear Stark shifts frequently found from defects in *h*-BN, we revealed possible out-of-plane tilts in the atomic bonding angle of SPE through comparison with first-principles calculations, providing insights on the mirror symmetry breaking in SPE necessary to understand their optical properties. In addition to the field-induced energy shift, the application of electric fields is found to be potentially useful in modifying the charge state of defects. Altogether, our results on electrical control of single defects in *h*-BN show the potential of 2D materials for tunable room temperature solid-state emitters, which are well-suited for free-space quantum communication and photonic quantum information processing.

Methods. *Measurements.* For optical measurements, we used a continuous-wave 532 nm laser for the excitation source that is focused onto the sample by an objective lens (NA = 0.6) with laser power of 0.16−1.6 mW. The emitted light is collected by the same objective lens, passed through a long-pass filter, and was detected by a spectrometer equipped with CCD detector. For $g^{(2)}(\Delta t)$ measurements, we directed the emitted light through an additional band-pass filter and two avalanche photodiodes (Excelitas Technologies) connected to a time-correlated single-photon counting module (qutools, quTAU). For polarization-dependent measurements, two Glan−Taylor linear polarizers and an achromatic half-wave plate are inserted in the optical path. For the electrical control, a gate voltage no greater than ±80 V is applied to the defects during the experiments to prevent the breakdown of the fabricated devices.

Simulations. We performed DFT calculations with a semilocal PBE functional[28] using plane-wave basis sets (with a cutoff energy of 85 Ry), optimized norm-conserving Vanderbilt (ONCV) pseudopotentials[29,30] and the QUANTUM ESPRESSO code.[31] The primary defects that we considered are neutral V_NX_B (X = C, N, or B) in isolated forms. To mimic the presence of an isolated defect in a single *h*-BN layer within the periodic boundary condition, we employed a 60-atom supercell (in-plane dimensions of 12.6 Å × 13.1 Å), in which a *h*-BN sheet is separated from its periodic images by a 16 Å thick vacuum space. We sampled the Brillouin zone with the Γ point only. We applied an out-of-plane electric field by using the sawtooth potential method along with the dipole correction.[32] All of the defects considered were fully relaxed. The ZPL of the V_NX_B defects was calculated using the ΔSCF method.[33] The defect-level diagrams and the defect orbitals of the V_NX_B defects are described in Figure S8. Numerical convergence in terms of the supercell size, the plane-wave cutoff energy, and the vacuum thickness were thoroughly examined (Figure S9), and we found that the ZPL shift converges within 0.1 nm using our numerical set-ups.

■ ASSOCIATED CONTENT

Supporting Information

The Supporting Information is available free of charge on the ACS Publications website at DOI: 10.1021/acs.nanolett.8b01030.

Figures showing device microscope images, power saturation, linear and other types of Stark shifts, second-order correlations, defect-level diagrams, convergence tests, device structures, spectral measurements, and discrete modification of emission intensity. (PDF)

■ AUTHOR INFORMATION

Corresponding Author

*E-mail: jelee@ajou.ac.kr.

ORCID

Jieun Lee: 0000-0002-3312-6369

DOI: 10.1021/acs.nanolett.8b01030
Nano Lett. 2018, 18, 4710−4715

Notes

The authors declare no competing financial interest.

■ ACKNOWLEDGMENTS

This work was supported by the "New Faculty Research Fund" of Ajou University and "Human Resources Program in Energy Technology" of the Korea Institute of Energy Technology Evaluation and Planning (KETEP) and was granted financial resources from the Ministry of Trade, Industry & Energy, Republic of Korea. (grant no. 20164030201380). H.S. was supported by the National Research Foundation of Korea (NRF) grant funded by the Korea government (MSIT) (no. 2017R1C1B5077000).

■ REFERENCES

(1) Geim, A. K.; Grigorieva, I. V. *Nature* **2013**, *499*, 419.
(2) Mak, K. F.; Shan, J. *Nat. Photonics* **2016**, *10*, 216−226.
(3) Chakraborty, C.; Kinnischtzke, L.; Goodfellow, K. M.; Beams, R.; Vamivakas, A. N. *Nat. Nanotechnol.* **2015**, *10*, 507−511.
(4) Koperski, M.; Nogajewski, K.; Arora, a.; Cherkez, V.; Mallet, P.; Veuillen, J.-Y.; Marcus, J.; Kossacki, P.; Potemski, M. *Nat. Nanotechnol.* **2015**, *10*, 503−506.
(5) He, Y.-M.; Clark, G.; Schaibley, J. R.; He, Y.; Chen, M.-C.; Wei, Y.-J.; Ding, X.; Zhang, Q.; Yao, W.; Xu, X.; et al. *Nat. Nanotechnol.* **2015**, *10*, 497−502.
(6) Srivastava, A.; Sidler, M.; Allain, A. V.; Lembke, D. S.; Kis, A.; Imamoğlu, A. *Nat. Nanotechnol.* **2015**, *10*, 491−496.
(7) Tran, T. T.; Bray, K.; Ford, M. J.; Toth, M.; Aharonovich, I. *Nat. Nanotechnol.* **2015**, *11*, 37.
(8) Martinez, L. J.; Pelini, T.; Waselowski, V.; Maze, J. R.; Gil, B.; Cassabois, G.; Jacques, V. *Phys. Rev. B: Condens. Matter Mater. Phys.* **2016**, *94*, 121405.
(9) Chejanovsky, N.; Rezai, M.; Paolucci, F.; Kim, Y.; Rendler, T.; Rouabeh, W.; Oliveira, F. F.; de Herlinger, P.; Denisenko, A.; Yang, S.; et al. *Nano Lett.* **2016**, *16*, 7037.
(10) Jungwirth, N. R.; Calderon, B.; Ji, Y.; Spencer, M. G.; Flatté, M. E.; Fuchs, G. D. *Nano Lett.* **2016**, *16*, 6052−6057.
(11) Choi, S.; Tran, T. T.; Elbadawi, C.; Lobo, C.; Wang, X.; Juodkazis, S.; Seniutinas, G.; Toth, M.; Aharonovich, I. *ACS Appl. Mater. Interfaces* **2016**, *8*, 29642−29648.
(12) Tran, T. T.; Elbadawi, C.; Totonjian, D.; Lobo, C. J.; Grosso, G.; Moon, H.; Englund, D. R.; Ford, M. J.; Aharonovich, I.; Toth, M. *ACS Nano* **2016**, *10*, 7331−7338.
(13) Grosso, G.; Moon, H.; Lienhard, B.; Ali, S.; Efetov, D. K.; Furchi, M. M.; Jarillo-Herrero, P.; Ford, M. J.; Aharonovich, I.; Englund, D. *Nat. Commun.* **2017**, *8*, 705.
(14) Chakraborty, C.; Goodfellow, K. M.; Dhara, S.; Yoshimura, A.; Meunier, V.; Vamivakas, A. N. *Nano Lett.* **2017**, *17*, 2253−2258.
(15) Xia, F.; Wang, H.; Xiao, D.; Dubey, M.; Ramasubramaniam, A. *Nat. Photonics* **2014**, *8*, 899−907.
(16) Aharonovich, I.; Englund, D.; Toth, M. *Nat. Photonics* **2016**, *10*, 631−641.
(17) Wang, L.; Meric, I.; Huang, P. Y.; Gao, Q.; Gao, Y.; Tran, H.; Taniguchi, T.; Watanabe, K.; Campos, L. M.; Muller, D. A.; et al. *Science* **2013**, *342*, 614−618.
(18) Lounis, B.; Orrit, M. *Rep. Prog. Phys.* **2005**, *68*, 1129−1179.
(19) Tamarat, P.; Gaebel, T.; Rabeau, J. R.; Khan, M.; Greentree, A. D.; Wilson, H.; Hollenberg, L. C. L.; Prawer, S.; Hemmer, P.; Jelezko, F.; et al. *Phys. Rev. Lett.* **2006**, *97*, 83002.
(20) Abdi, M.; Hwang, M. J.; Aghtar, M.; Plenio, M. B. *Phys. Rev. Lett.* **2017**, *119*, 233602.
(21) Abdi, M.; Chou, J.-P.; Gali, A.; Plenio, M. B. *ACS Photonics* **2018**, *5*, 1967.
(22) Sajid, A.; Reimers, J. R.; Ford, M. J. *Phys. Rev. B: Condens. Matter Mater. Phys.* **2018**, *97*, 064101.
(23) Wu, F.; Galatas, A.; Sundararaman, R.; Rocca, D.; Ping, Y. *Phys. Rev. B* **2017**, *1*, No. 071001(R).
(24) Reimers, J. R.; Sajid, A.; Kobayashi, R.; Ford, M. J. *J. Chem. Theory Comput.* **2018**, *14*, 1602−1613.
(25) Tawfik, S. A.; Ali, S.; et al. *Nanoscale* **2017**, *9*, 13575−13582.
(26) Jungwirth, N. R.; Fuchs, G. D. *Phys. Rev. Lett.* **2017**, *119*, 057401.
(27) De Las Casas, C. F.; Christle, D. J.; Ul Hassan, J.; Ohshima, T.; Son, N. T.; Awschalom, D. D. *Appl. Phys. Lett.* **2017**, *111*, 262403.
(28) Perdew, J. P.; Burke, K.; Ernzerhof, M. *Phys. Rev. Lett.* **1996**, *77*, 3865−3868.
(29) Hamann, D. R. *Phys. Rev. B: Condens. Matter Mater. Phys.* **2013**, *88*, 85117.
(30) Schlipf, M.; Gygi, F. *Comput. Phys. Commun.* **2015**, *196*, 36−44.
(31) Giannozzi, P.; Baroni, S.; Bonini, N.; Calandra, M.; Car, R.; Cavazzoni, C.; Ceresoli, D.; Chiarotti, G. L.; Cococcioni, M.; Dabo, I.; et al. *J. Phys.: Condens. Matter* **2009**, *21*, 395502.
(32) Bengtsson, L. *Phys. Rev. B* **1999**, *59*, 301−304.
(33) Seo, H.; Ma, H.; Govoni, M.; Galli, G. *Phys. Rev. Mater.* **2017**, *1*, 75002.

DOI: 10.1021/acs.nanolett.8b01030
Nano Lett. 2018, 18, 4710−4715